Single-station moment tensor inversion on Mars

Nienke Brinkman[1], Simon C. Stähler[1], Domenico Giardini[1], Cedric Schmelzbach[1], Alice Jacob[2], Nobuaki Fuji[2], Clement Perrin[2], Philippe Lognonne[2], Maren Böse[1], Brigitte Knapmeyer-Endrun[3], Eric Beucler[4], Savas Ceylan[1], John F. Clinton[3], Constantinos Charalambous[5], Martin van Driel[1], Fabian Euchner[1], Anna Horleston[6], Taichi Kawamura[7], Amir Khan[1], Guenole Mainsant[8], Mark P. Panning[9], William. T. Pike[5], John-Robert Scholz[10], Johan O. A. Robertsson[1], William B. Banerdt[9]

[1]Institute of Geophysics, ETH Zürich, Sonneggstrasse 5, 8092 Zürich, Switzerland
[2]Université de Paris, Institut de physique du globe de Paris, Paris, France
[3]Bensberg Observatory, University of Cologne, Bergisch Gladbach, Germany.
[4]Laboratoire de Planétologie et Géodynamique, UMR6112, Univ. Nantes, Univ. Angers, CNRS, 2 rue de la Houssinière - BP 92208, 44322 Nantes Cedex 3, France
[9]NASA Jet Propulsion Laboratory, California Institute of Technology, Pasadena, USA,
[6]School of Earth Sciences, University of Bristol, Wills Memorial Building, Queens Road, Bristol BS8 1RJ, UK
[7]Université de Paris, Institut de physique du globe de Paris, CNRS, F-75005 Paris, France
[8]Institut Supérieur de l'Aéronautique et de l'Espace SUPAERO, 10 Avenue Edouard Belin, 31400 Toulouse, France
[5]Department of Electrical and Electronic Engineering, Imperial College London, South Kensington Campus, London, SW7 2AZ, United Kingdom
[10]Max Planck Institute for Solar System Research, Justus-von-Liebig-Weg 3, 37077 Göttingen, Germany

Key Points:

- We present new a method for single station moment tensor inversion
- The method is applied to marsquakes recorded by InSight
- We find dominantly normal faulting style

Corresponding author: Nienke Brinkman, nienke.brinkman@erdw.ethz.ch

Abstract

In early 2019, NASA's InSight lander successfully deployed a single three-component very broadband seismometer (VBB) on the surface of Mars to detect and characterize marsquakes. Using these data, we present a method to infer the source mechanisms of marsquakes from waveforms of P and S waves recorded at a single station. We show that the three events with the highest signal-to-noise ratio (SNR) and a robust distance estimate S0173a, (May 23rd 2019), S0235b, (July 27th 2019) and S0183a, (June 3rd 2019) are all likely the results of normal faulting, suggesting an extensional regime mainly oriented south-east north-west in the respective source regions, Cerberus Fossae and Orcus Patera. We quantify the uncertainty of our solutions by comparing results of a direct inversion with a grid-search method.

Plain Language Summary

As time passes, the mysterious interior of Mars is slowly being unraveled thanks to the detection and analysis of marsquakes with a seismograph carried by the InSight lander. Over 300 marsquakes have so far been identified, yet only a handful of those show similarities to earthquakes. Those earth-like events are located near the Cerberus Fossae and Orcus Patera regions. We take advantage of the marsquakes showing similarities with earthquakes by applying a methodology developed for earthquake characterization before the abundance of recorders on Earth. We find that the marsquakes in these source regions are dominated by Mars pulling apart rather than compressing. This is important information to further understand what causes these marsquakes.

1 Introduction

On the 26th of November 2018, NASA's InSight lander successfully touched down on the martian surface in Elysium Planitia. Among other instruments the lander transported a single three-component very broadband seismometer (VBB) to measure seismic events (Lognonné et al., 2019). These measurements are used to determine the seismic activity level and eventually the internal structure of Mars. Up to December 31st 2019, 383 seismic events have been detected by the Marsquake service (MQS) (InSight Marsquake Service, 2020; J. Clinton et al., 2018) and assigned to different classes (Banerdt et al., 2020; Giardini et al., 2020; Lognonné et al., 2020). In this work, we infer the source mechanisms of three marsquakes with the highest signal-to-noise ratio (SNR) and a robust distance estimate that are part of the low frequency family of events (InSight Marsquake Service, 2020). These marsquakes occurred on solar day (sol) 173 (event S0173a, May 23rd 2019), 183 (event S0183a, June 3rd 2019) and 235 (event S0235b, July 27th 2019). The MQS located these events in the vicinity of the Cerberus Fossae and Orcus Patera regions (Giardini et al., 2020), as illustrated in Figure 1.

From imaging faults, detailed studies on their systems and potentially seismically induced rock falls, Cerberus Foassae had been considered a primary seismically active region on Mars before landing (Knapmeyer et al., 2006; Taylor et al., 2013; Roberts et al., 2012). Both events S0173a and S0235b are located close to this region. Moment tensor solutions offer additional insights in establishing the dominant source mechanism by revealing the fault type and fault orientations, but it is difficult with sparse networks or single stations . Moment tensor inversion with the Apollo dataset recorded on the moon has not been possible, mainly due to the high amount of scattering in the seismic data (Knapmeyer & Weber, 2010).

Since we are limited to a single-station source inversion, it is necessary to extract as much information as possible out of one seismogram. Earlier terrestrial approaches in single station source inversion were mainly based on surface waves (Giardini et al., 1993, 1994), however surface waves have as of yet not been identified in the InSight seis-

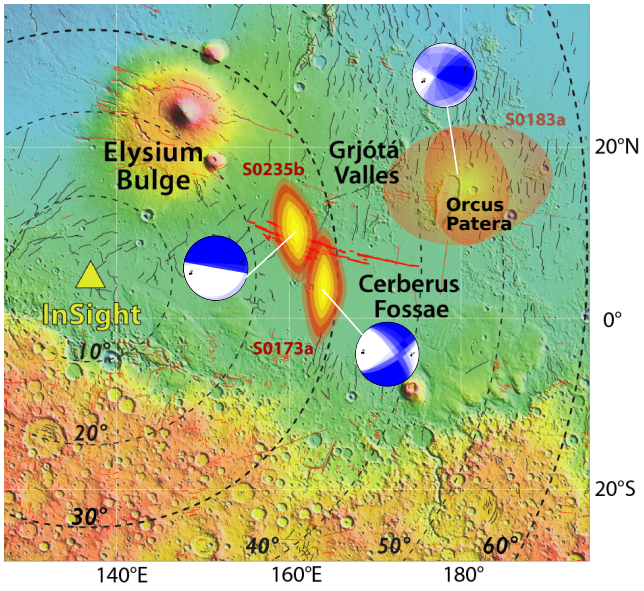

Figure 1. Mars Orbiter Laser Altimeter shaded relief of Elysium Planitia from (Giardini et al., 2020). The location of the InSight lander (yellow triangle) is illustrated with respect to events S0235b (latitude: 11° & longitude: 161°), S0173a (latitude: 3° & longitude: 165°) and S0183a (latitude: 23° & longitude: 177°). The ellipsoids indicate distance uncertainties on the source location. Black and red lines present reverse and normal mapped faults, respectively. Probabilistic beach ball solutions determined for each marsquake point towards their location.

mic dataset (Giardini et al., 2020). Accordingly, we use the waveforms of P and S phases (direct phases) of the VBB data (InSight Mars SEIS Data Service, 2019) to solve the inverse problem of seismic sources, an approach that has been used in multi-station settings on earth (Kennett et al., 2000; Vallée et al., 2011; Garcia et al., 2013; S. Stähler & Sigloch, 2014; S. C. Stähler & Sigloch, 2016). We propose a thorough characterization approach that includes a substantial amount of tests to obtain a stable source solution. We use simultaneously a direct inversion and a grid-search method to ensure a valid solution. These methods attempt to fit synthetic waveforms with the observed waveforms. The direct P and S wave trains of event S0173a and S0235b show a clear P and S arrival and a distinct polarization. Therefore, both direct phases are confidently used for the source inversion. For event S0183a no S waves are observed with high certainty. Therefore, inference of the focal mechanism associated with this event is performed using solely P waves.

2 Data

We determine the focal mechanism of only three high quality low frequency marsquakes, discussed in the introduction, due to their Earth-like characteristics. This allows us to apply methodologies that are developed for Earth on marsquakes. The distance, back-azimuth (BAZ) and location were estimated by the MQS (InSight Marsquake Service, 2020) using methods described in Khan et al. (2016); Böse et al. (2017); J. Clinton et al. (2018). The distance and BAZ for each event are listed in Table 1 and their location is specified in the caption of Figure 1.

We use the continuous seismic records of the VBB sampled at 20 Hz and rotate the axes to their vertical (Z), radial (R) and transverse (T) components. The back azimuth

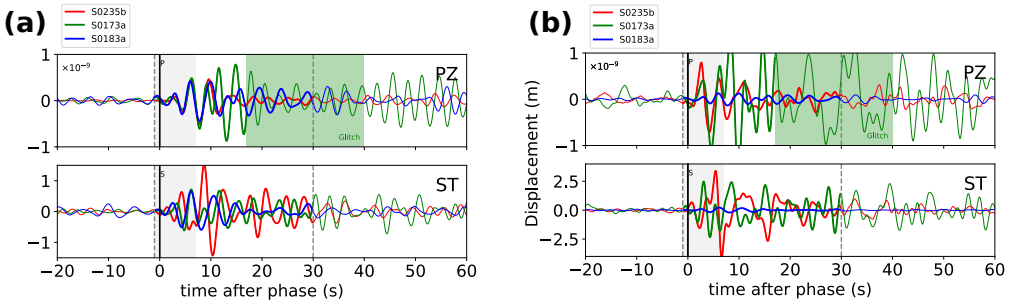

Figure 2. A comparison of seismograms for the three events discussed in this paper. **(a)** A band-pass filter of 0.2-0.4 Hz applied to the data and each event is scaled to fit the maximum absolute amplitude of the first 7 seconds of event S0235b. **(b)** Original data passed through their individual band-pass filter that is specified in Table 1. The recordings of events S0235b, S0173 and S0183a are illustrated in red, green and blue, respectively. The gray dashed lines represent the start and end of the inversion window. The black solid lines illustrate the P and S phase arrivals. The light-gray and light-green area represent the higher weighted part of the waveform and the glitch recording for event S0173a, respectively.

is used to construct the rotated components. To determine the source solutions, we select a 30 second time window around each phase pick (P and S) on all components except the T component of the P phase, because P wave energy does not arrive on the T component. Figure 2 illustrates the windowed P wave on the Z component (PZ) and the S wave on the T component (ST) recordings of the three marsquakes shown with bold colored lines. Extra weight is added to the first 7 seconds of the window, indicated by the light-gray area, forcing the inversion to prioritize fitting the first polarity of the waveforms. The additional coda included in the inversion is, however, crucial to stabilize the source solution such that solutions at the nodal planes are avoided, because these nodal plane solutions are extremely unstable. The green box highlights a glitch, an artifact of the seismometer described in Scholz et al. (2020), in the recorded data of S0173a, therefore this part of the recordings is excluded from the inversion.

Figure 2 shows the available data of the three marsquakes. Figure 2a shows the marsquake recordings overlapped in amplitude and filtered with a band-pass filter of 0.2-0.4 Hz to be able to compare the P and S polarities of the events. The amplitude scaling is applied to amplify the relatively weak S wave amplitude in the original data of event S0183a. The first 7 seconds of PZ is very similar for all three marsquakes. Yet, event S0235b shows dissimilarities on ST for the first 7 seconds with respect to event S0173a and S0183a. The comparable initial polarities of PZ and ST for event S0173a and S0183a indicate source solutions of the same kind.

Figure 2b illustrates the original data, where each event is filtered with a band-pass filter that is specified in Table 1. These band-pass filters pass the highest energy for both P and S body waves to emphasize the onset of the phase arrival and are used for the source inversion.

3 Inversion approaches

For our direct inversion and grid-search method, we incorporate prior knowledge (reproduced in Table 1) on the location, origin time and phase arrival times for each event provided by the MQS to condition the inverse problem. We consider five different parts of the waveform of each 30 seconds to infer the source solutions. The seismograms are

Table 1. Event and pre-processing parameters.

Source Parameters	**S0235b**	**S0173a**	**S0183a**
Event quality	A	A	C
BAZ	74°	91°	61°
Epicentral distance	25°	29°	43°
Origin Date	2019-07-26	2019-05-23	2019-06-03
Origin Time	12:16:15	02:19:33	02:22:17
P-Pick	12:19:19	02:22:59	02:27:45
S-Pick	12:22:06	02:25:54	02:32:09
Mw	3.6 (M0 = 3.16e+14)	3.6 (M0 = 3.16e+14)	3.1 (M0=5.62e+13)
Bodywave attenuation (t^*)	P: 1.2 S: 1.5	1.2 1.6	1.2 -
Bandpass corner frequencies (Hz)	0.1– 0.9	0.1 – 0.7	0.2 – 0.4

filtered with a non-zero-phase fourth order band-pass butterworth filter. The corner frequencies of the band-pass filter applied to each event are specified in Table 1.

Both inversion methods fit synthetic waveforms to the 3 component marsquake data. Synthetic seismograms are extracted from a broadband waveform database (Instaseis) down to a period of 1 second. This database uses precomputed waveform simulations and interpolation to synthesize high-fidelity seismic recordings much faster than wavefield simulation can achieve (Nissen-Meyer et al., 2014; Van Driel et al., 2015). The seismograms are generated using synthetic data corresponding to a pre-existing purely layered velocity model. We apply two of these models for our source inversions, shown in Figure A1. These velocity models are based on general assumptions of the bulk chemistry, mineralogy and geotherm from previous studies established mainly from Martian meteorites (Khan & Connolly, 2008; Rivoldini et al., 2011; Khan et al., 2018) and instaseis databases for those are publicly available (J. F. Clinton et al., 2017; Ceylan et al., 2017). The first model includes new upper-crustal layering information based on estimated receiver functions (Lognonné et al., 2020) to explain the slightly earlier arrivals of the S waves on the R and T component with respect to the Z component. The crustal thickness of this model is expected to be relatively thin, where the Moho is located at 24 km depth. The second model that we used consists of a thick crust (Moho at 77 km). These two dissimilar velocity models can therefore be used to assess the stability of the source solution with respect to crustal thickness.

The synthetic seismograms are computed in a purely elastic velocity model and convolved with a source time function (STF) simulating the effect of body wave attenuation. This is defined for both P and S by integrating the quality factor (Q) over the ray path of the seismic phase, which is expressed in terms of the t^* value. The t^* values for both P and S phases for each marsquake are specified in Table 1.

3.1 Direct inversion

Our direct inversion method solves the inverse problem of seismic sources using a linear time domain moment tensor inversion. The synthetic data are constructed by multiplying Green's function components corresponding to an impulse response at the source

location with the individual moment tensor components. This can be captured in a matrix-vector product

$$\mathbf{d_{obs}} = G\mathbf{m} \tag{1}$$

where G and $\mathbf{m}$ represent the Green's function matrix and a vector representation of the moment tensor components, respectively. We use Equations 6,7 and 8 from Minson and Dreger (2008) to define our Green's function. The isotropic component of the moment tensor is assumed to be zero, which allows us to express the moment tensor in terms of five independent components. We can compute a generalized inverse using a stacked version of the data and their corresponding fundamental Green's function to estimate the individual moment tensor components:

$$\mathbf{m_{est}} = (G^T C_d^T C_d G)^{-1} G^T C_d^T C_d \mathbf{d_{obs}} \tag{2}$$

where $\mathbf{m_{est}} = [m_{xx}, m_{yy}, m_{xy}, m_{xz}, m_{yz}]^T$ represent the 5 independent components of the moment tensor. C_d is the data covariance matrix that incorporates the standard deviation, σ, of a 30 second window before the phase arrival on each component. Because each trace has an individual σ value, the covariance matrix is a block diagonal matrix constructed from 5 individual unit matrices multiplied with the relevant σ^2 value. As mentioned before, we apply more weight to the first 7 seconds of the data (i.e. 140 samples) using a weighting factor w that is 1 for the first 7 seconds and 3 for the rest of the trace. The value of 3 was found to be a good compromise between stability and quality of fit. Thus, C_d is given by

$$C_d(k + i \times nt, k + i \times nt) = \sigma_i^2 \mathbf{w}_k \tag{3}$$

where k represents the number of samples, i refers to the number of traces and nt is equal to the length of the traces.

Finally, we decompose the moment tensor into its double-couple (DC) and compensated linear vector dipole (CLVD) component following Jost and Herrmann (1989). By assuming the isotropic component to be zero and using only a single-station, we use the CLVD component as a measure of stability. The moment tensor is splitted into an isotropic and deviatoric component expressed in terms of the eigenvectors and eigenvalues to perform the decomposition. The ratio between the minimum and maximum eigenvalue, respectively e_{min} and e_{max}, represents the measure of DC component with respect to the CLVD component:

$$\epsilon = \frac{|e_{\min}|}{e_{\max}}. \tag{4}$$

Thus, ϵ provides information on the energy ratio of CLVD to DC in the moment tensor.

The DC part of the moment tensor solution is used to compute synthetic waveforms such that it is possible to calculate a measure of fit based on a sample-wise difference between the observed and synthetic data, i.e. the ℓ_2-norm (misfit):

$$\chi^2 = \frac{1}{2}(\mathbf{d_{obs}} - \mathbf{d_{syn}})^T C_d^{-1} (\mathbf{d_{obs}} - \mathbf{d_{syn}}) \tag{5}$$

where $\mathbf{d_{obs}}$ and $\mathbf{d_{syn}}$ represent the selected part of the observed and synthetic waveform used for the inversion, respectively.

3.2 Grid-search method

A grid-search (GS) method was developed to systematically explore the model space for purely double-couple sources to validate the DC source solutions obtained from the direct inversion. The moment tensor is expressed in terms of 4 independent components: the scalar moment (M0) and the three unique orientation angles, strike (ϕ), dip (δ) and rake (λ). In this study the up-south-east (USE) coordinate system convention with up

198 (r), south (θ) and east (ϕ) is used. We investigate a range of fault angle combinations
199 with a 20° interval for the strike angle and a 15° interval for the dip and rake angle. For
200 each step in the GS method a scaling factor between the envelopes of the observed and
201 synthetic waveforms is calculated and used to re-scale the synthetic waveform. This scal-
202 ing factor is directly linked to the scalar moment (M0) estimation

$$M0 = \frac{1}{2} \cdot \frac{\sum |\mathbf{d_{obs,PZ}} + \mathbf{d_{obs,ST}}|}{\sum |\mathbf{d_{syn,PZ}} + \mathbf{d_{syn,ST}}|} \tag{6}$$

203 We choose only the PZ and ST trace to estimate M0 as they should represent the P and
204 S phase arrivals the clearest. For each point in the grid search we calculate the misfit
205 using Equation 5, where d_{syn} is re-scaled by the estimated $M0$ determined in Equation 6.
206 We store the ten orientation angle combinations that result in the lowest misfit.

207 4 Implementation

208 The misfit measure calculated in Equation 5 expects, on average, an error between
209 observed and synthetic waveforms equal to the difference per sample. This measure de-
210 termines the variance reduction of the synthetic waveform with respect to the variance
211 of the noise.

212 To understand the impact of the source depth on both algorithms, we apply the
213 direct inversion and grid-search method to multiple depths ranging from 5 km to 90 km
214 with 3 km interval steps. For each depth interval we store a single optimal source solu-
215 tion calculated by the direct inversion and ten fault angle combinations that result in
216 the lowest misfit computed by the GS method. This allows us to compare the various
217 source solutions determined from both methods over depth.

218 Since we are limited to only a single-station, we tested different scenarios to eval-
219 uate the stability of the solutions. Here, we describe 5 of these. For each scenario, we
220 performed the GS and direct inversion at the mentioned depth range, i.e. 29 different
221 depths.

222 In addition, we implement a synthetic test to check the performance of the direct
223 inversion and GS method. We create events artificially and use the two methods to es-
224 timate the sources of these events. The results of these tests are illustated in Figure B1.

225 4.1 P and S wave inversion

226 Figures 3a and 3b show the source solutions for event S0235b and S0173a, respec-
227 tively. These solutions are inferred from inverting both P and S phases using the 1D struc-
228 tural model with a crustal thickness of 24 km (blue line in Figure A1).

229 Figures 3a and 3b show ten solutions with the lowest misfit value inferred from the
230 GS method computed at a depth of 56 km and 29 km, respectively. These depths are
231 selected based on relatively low misfit and epsilon values. Figure 3c and 3d illustrate the
232 optimal solution of the direct inversion computed at the same selected depths as in Fig-
233 ure 3a and 3b. Figures 3e and 3f show the trend of the misfit and the epsilon values with
234 depth.

235 4.2 P wave inversion

236 Solely P waves were used to infer the source solutions of event S0183a. Figures 4a
237 and 4b show the probabilistic beachballs together with the corresponding waveforms of
238 the ten GS solutions with the lowest misfit values at 29 km and 41 km depth for event
239 S0183a, respectively. We do not present the optimal source solution determined from the
240 direct inversion, since its solution is highly non-unique.

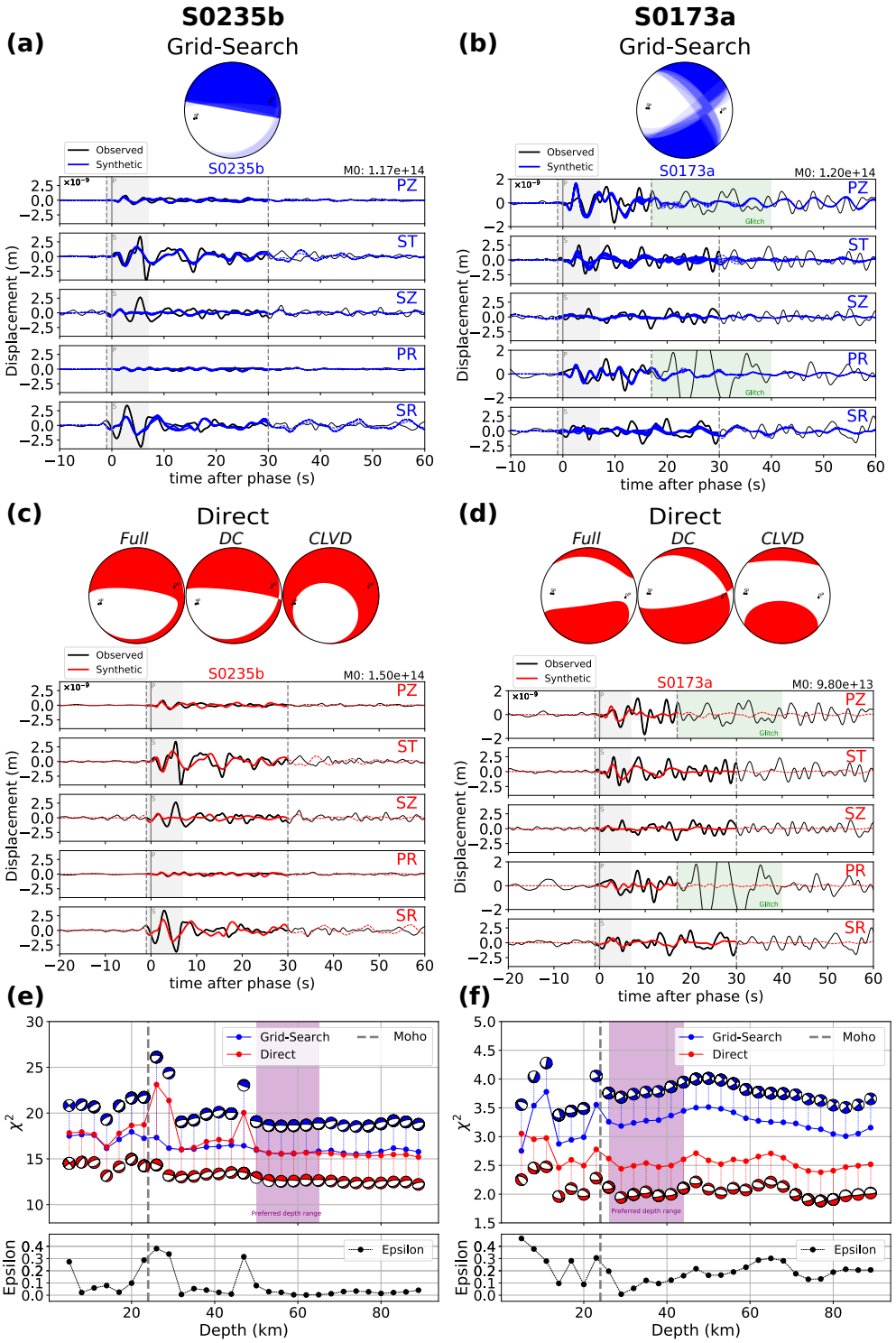

Figure 3. P and S wave inversion for a thin crustal model: Inversion results of the direct inversion (red) and GS method (blue) using a 24 km crustal thickness. Figure **(a)** and **(c)** and Figure **(b)** and **(d)** show results computed at 56 km and 29 km depth, respectively. **(a,b)**: A probabilistic beachball and the waveform representation of the 10 best solutions computed by the GS at the selected depth. The ray piercing-points of P, S and pP are indicated by the black dots in the beachball. Gray dashed lines in the waveform plot represent the start and end of the inversion window. Light-gray area represents the higher weighted part of the waveform. **(c,d)**: Focal mechanism and waveforms of the direct inversion. The beachballs from left to right: the full MT solution and decomposition into DC and the CLVD. **(e,f)**: The misfit and the epsilon values with depth. The blue and red beachballs show the source solutions belonging to their misfit values. The dashed gray line denotes the selected depth of the Moho and the purple area indicates the range of depths with preferred source solutions.

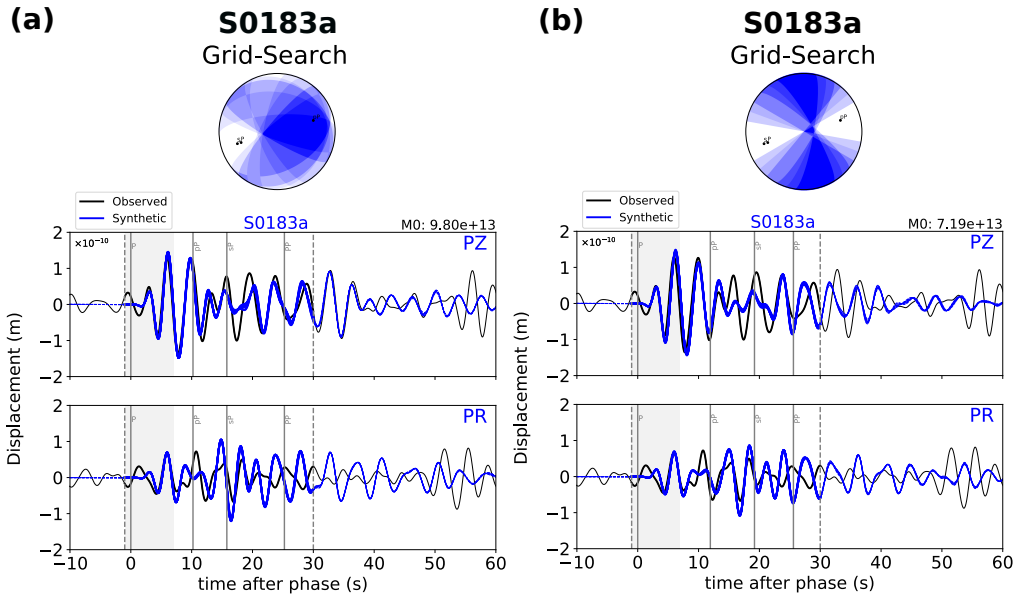

Figure 4. P wave inversion for a shallow crustal model: Inversion results of the GS method using a 24 km crustal model. Figure **(a)** and **(b)** show results computed at a depth of 29 km and 41 km, respectively. The probabilistic beachball and the waveform Figures are structured the same as in Figure 3a and 3b. The solid gray vertical lines denote the first arriving P and S phase and later arriving phases pP, sP and PP calculated using ray-tracing.

4.3 Varying crustal thicknesses

We assessed the influence of a larger crustal thickness (e.g. 77 km) on the stability of the source solutions. The results for this test are shown in Figure C1. The solutions for event S0235b remain stable over depth for a deep crustal model. Yet, the stability decreases closer to the Moho. The stability of the source solutions of event S0173a decreases using a deep crustal model compared to the results of the shallow crustal model. Accordingly, the epsilon values illustrated in Figure C1f increased compared to Figure 3f indicating a less reliable solution.

4.4 Including a S shadow-zone

As mentioned, only a few velocity models out of an extensive database proposed by the MQS show a stable match for S-P travel time differences. The majority of the unstable models predict an S wave shadow-zone starting around 20° (Giardini et al., 2020). To not exclude the possibility of such a S wave shadow-zone, we have tested the influence on the source solutions by interchanging the S phase arrival with a secondary SS phase arrival. The inferred source solutions of the direct inversion using P and SS waves are comparable with the solutions of inverting P and S waves. Yet, the GS solutions show to be unstable for the P and SS wave inversion.

4.5 Varying the band-pass filters

We investigated the the stability of the source solutions for event S0235b and S0173a by applying a more narrow band-pass filter with corner frequencies from 5 to 8 seconds. We present the inversion results of this test in Figure C3. The moment tensor solutions determined from these inversions remain very stable, especially below the Moho.

5 Results

In the following, we discuss our preferred source solutions of the three marsquakes (S0235b, S0173a and S0183a) resulting from the approach obtained in Section 4. For each event we select a depth range that comprises a set of stable solutions with relatively low misfit and epsilon values. Note that we present only the DC component of the source solution, which is characterized by two identical solutions: the fault plane and auxiliary plane solution. Our most stable (and thus preferred) source solutions are established from using a shallow crustal model. This is in agreement with recent findings on crustal information (Lognonné et al., 2020).

Additionally, we present the magnitude estimate for each marsquake for the selected depth range. These estimates deviate no more than a magnitude of 0.3 compared to the magnitude estimates determined in Giardini et al. (2020). The results that we present are based on a fixed epicenter provided by the MQS.

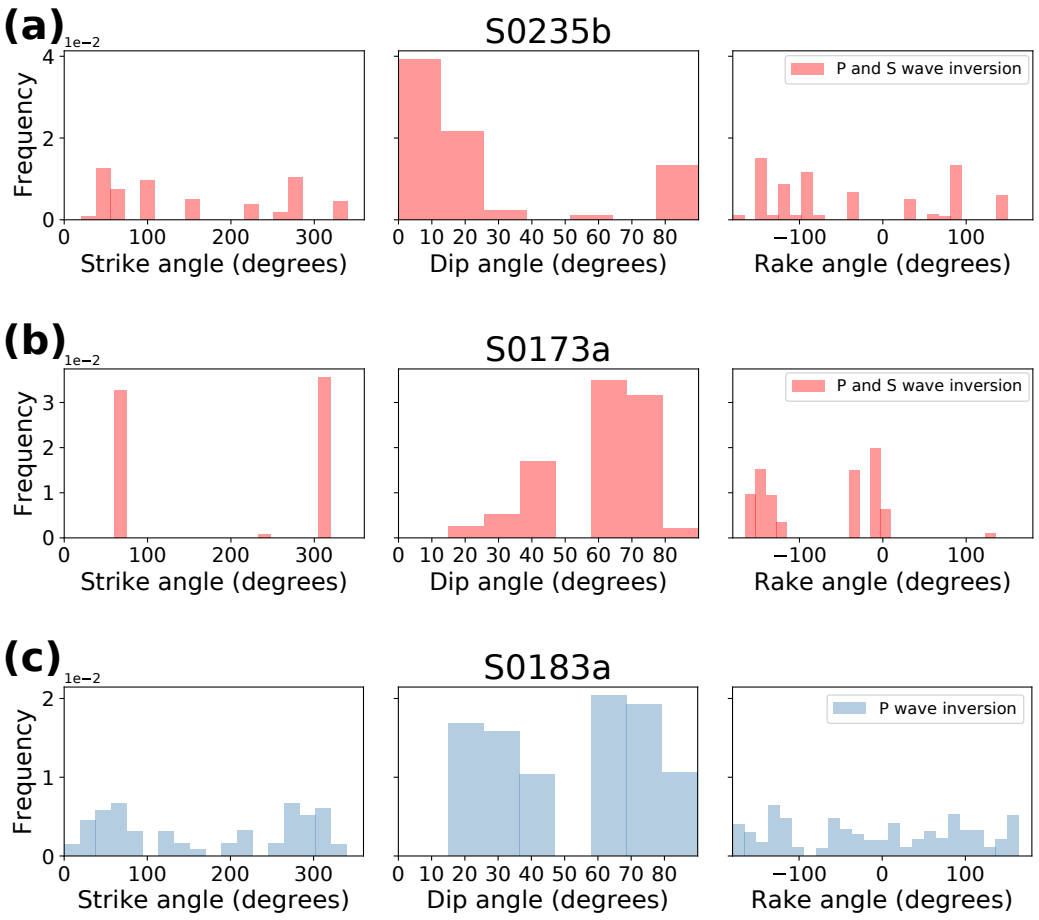

Figure 5. Histograms of the strike, dip and rake angle for the source solutions of the GS method determined from the preferred depth ranges. **(a)**: depth range from 50 km to 65 km for event S0235b, **(b)**: depth range from 26 km to 44 km for event S0173a and **(c)**: depth range from 26 km to 44 km for event S0183a. The frequency indicated on the Y-axis is normalized and weighted by the actual misfit values.

Table 2. The most frequent source solution illustrated in Figure 5.

Source solutions	**S0235b**	**S0173a**	**S0183a**
Strike	40	320	60
Dip	0	60	60
Rake	-150	-15	-135
Magnitude (M0)	3.3 (1.18e+14)	3.4 (1.65e+14)	3.3 (9.68e+13)

5.1 S0235b

The purple box in Figure 3e illustrates the desired depth range from 50 km to 65 km for a stable source solution of event S0235b. The parameters for the stable source solutions of the GS within this depth range are illustrated in the histogram shown in Figure 5a. We summed all the solutions within this depth range and weighted them by the exponent of the negative misfit value. The most frequent source solution is presented in Table 2. This result describes a west-east orientated dip-slip to normal fault regime.

5.2 S0173a

The purple box in Figure 3f illustrates the desired depth range from 26 km to 44 km for for a stable source solution of event S0235b. The parameters for the stable source solutions of the GS within this depth range are illustrated in the histogram shown in Figure 5b. Again, we summed all the solutions within this depth range and weighted them by the exponent of the negative misfit value. The most frequent source solution is presented in Table 2. This result describes a south-east north-west orientated normal fault regime.

5.3 S0183a

Event S0183a has a low S wave amplitude. The available structural models are not able to produce such a weak S wave signal given the estimated source location. Therefore, we invert solely P waves for this event to determine the source solution, see Figure 4. The beachballs solutions illustrate non-unique moment tensor solutions, which is expected from only inverting P waves.

Regardless the amplitude, the polarity of the P and the S wave of event S0183a and event S0173a are similar, as illustrated in Figure 2a. This provides an additional verification to the source solution of event S0183a due to an expected source solution comparable to event S0173a. We choose the same preferred depth range as event S0173a for event S0183a to define the source solutions. The preferred solutions is specified in Table 2 and Figure 5c. The corresponding fault regime, a south-east north-west orientated normal fault regime, is very similar to the regime determined for event S0173a.

6 Discussion

Our inversion methods are focused on fitting the first 7 seconds of the waveforms, because after those 7 seconds other phases arrive (e.g. depth phases, secondary phases, etc.) that are highly dependent on the structural model. Some of these later phase arrivals are emphasized with vertical gray lines in Figure 4. These phases are key to determine the event depth. In our current approach, it is therefore not feasible to determine the depth of the marsquakes. Yet, we do have a preference for an event depth be-

low the Moho, as the source solution stabilizes below the Moho regardless of the absolute depth. Additionally, a thin crust is favored over a thick crust based on the fact that for the latter waveform fits are significantly worse for later arriving phases consistent with results from Lognonné et al. (2020). Note, however, that these later arriving phases (after 7 seconds) are not included to constrain the source solution. Future work is needed to further constrain the crustal model with the information from these marsquakes by tracking down the later arriving phases in the waveform coda.

We interpret event S0235b to originate at a deeper depth than event S0173a due to the latter's more complex coda, possibly resulting from being closer to a reflecting interface, e.g. the Moho. The fact that higher amplitude waveforms arrive directly after the P wave for event S0173a strongly suggest that reflection/refraction phases are generated from a nearby discontinuity. This is not observed for event S0235b.

7 Conclusion

In this work, we show that it is possible to obtain a stable source solution from the recordings of a single three-component very broadband seismometer. Additionally, we find that three low frequency marsquakes are all likely the results of normal faulting with a relatively steep dipping fault plane. This suggest an extensional regime mainly oriented south-east north-west in the respective source regions of the events, Cerberus Fossae and Orcus Patera. We quantified the uncertainty of our solutions by comparing results of a direct inversion with a grid-search method. We extensively tested the influence of critical parameters (e.g. depth, structural model, filter parameters, etc.) on the stability of the source solutions. The solutions are relatively stable regardless of varying the depth and structural model, but all prefer a thin crust and an event depth below the Moho.

Appendix A Velocity models

Here, we illustrate the structural velocity models that we used to infer the source solution of the marsquakes. Figure A1 presents two models with a shallow and a deep crust provided by the MQS. The thin crustal model (shown in blue) includes additional upper-crustal layering information based on recent receiver functions estimates.

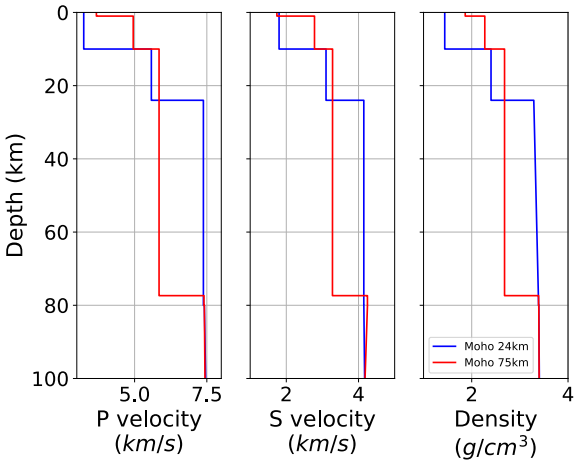

Figure A1. The P and S velocity and density of the first 100 km are illustrated for a thin and thick crustal model in blue and red, respectively. The thin crustal model includes upper-crustal layering information based on estimated receiver functions (Lognonné et al., 2020)

Appendix B Synthetic test

We have tested the performance of the two source inversion methods on an event created synthetically, added with real Martian noise. We choose a synthetic event rather than an Earth event, because the tuning parameters for Mars and Earth events are incompatible.

The synthetic test event used here is located close to event S0235b with a latitude of 11° and a longitude of 170° at a depth of 45 km. The magnitude is Mw 3.1. The location of the recording station is identical to InSight lander. The 1D-velocity model used to create this synthetic event corresponds to the shallow crustal velocity model with the Moho at 24 km that we have used for the marsquake inversions as well, see Figure A1. We added noise to the synthetic seismograms to simulate real data. The noise corresponds to actual Martian noise recorded with the VBB during one sol.

To test the performance of our inversion methods we invert events with different source mechanisms. Here, we show two main source types, a normal and a strike-slip fault, defined with a fixed dip and rake angle. We vary the strike angle, which is equivalent to changing the epicentral distance. Thus, we explore the influence of source-receiver location on the source solutions. Additionally, we analyse the effect of assuming an incorrect depth on the source solutions.

Figures B1a and B1b represent the inferred source solutions for respectively a pure normal fault and a pure strike-slip fault both with a strike angle of 60°. The gray dashed line indicates the Moho depth and the green dashed line represents the true depth of the event.

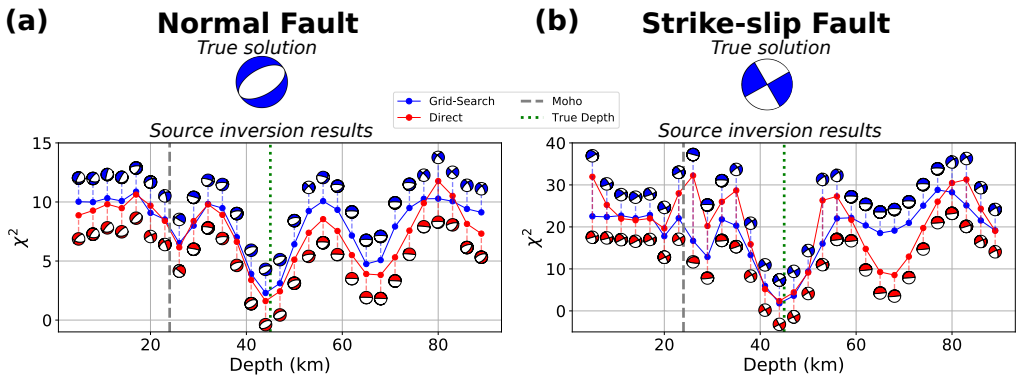

Figure B1. The inversion results of the direct inversion (red) and GS method (blue) of **(a)** a normal fault system and **(b)** a strike-slip fault system both with a strike angle of 60°. The blue and red beachballs show the source solutions belonging to their misfit values. The dashed gray line denotes the selected depth of the Moho and green dotted line illustrates the "true" depth location.

Appendix C Test results

To analyse the effect of a deep crustal model on the stability of the source solutions we invert the three Marsquakes with a 1D structural model with the MOHO at 77 km depth. Figures C1a, C1b and C2 show the inversion results for event S0235b, S0173a and S0183a, respectively. Figure C1a and C1c illustrate respectively the GS and direct inversion results at a depth of 56 km. Figure C1b and C1d show inversion results at a depth of 29 km. Figure C2a and C2b show GS results at a depth of 29 km and 41 km, respectively.

Additionally, we show the result of applying a narrow band-pass filter with corner frequencies of 0.125 Hz and 0.2 Hz in Figure C3. The source solutions are very similar to the solutions obtained from a wider band-pass.

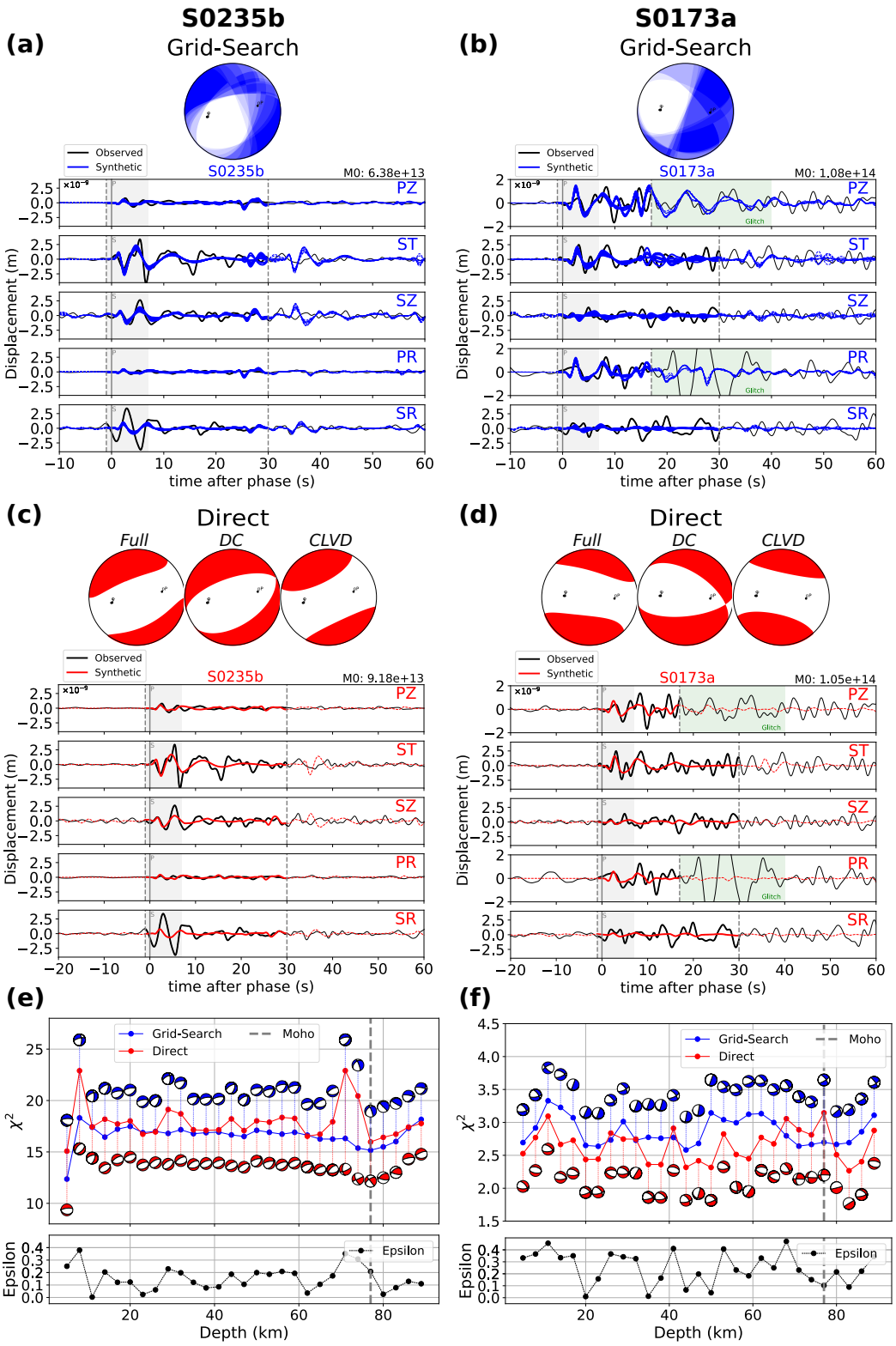

Figure C1. P and S wave inversion using a deep crustal model: Inversion results of the direct inversion (red) and GS method (blue) using a 77 km crustal model. **(a)**,**(c)** and **(b)**,**(d)** show results computed at 56 km and 29 km depth, respectively. **a-f** contain the same plot structure as in Figure 3.

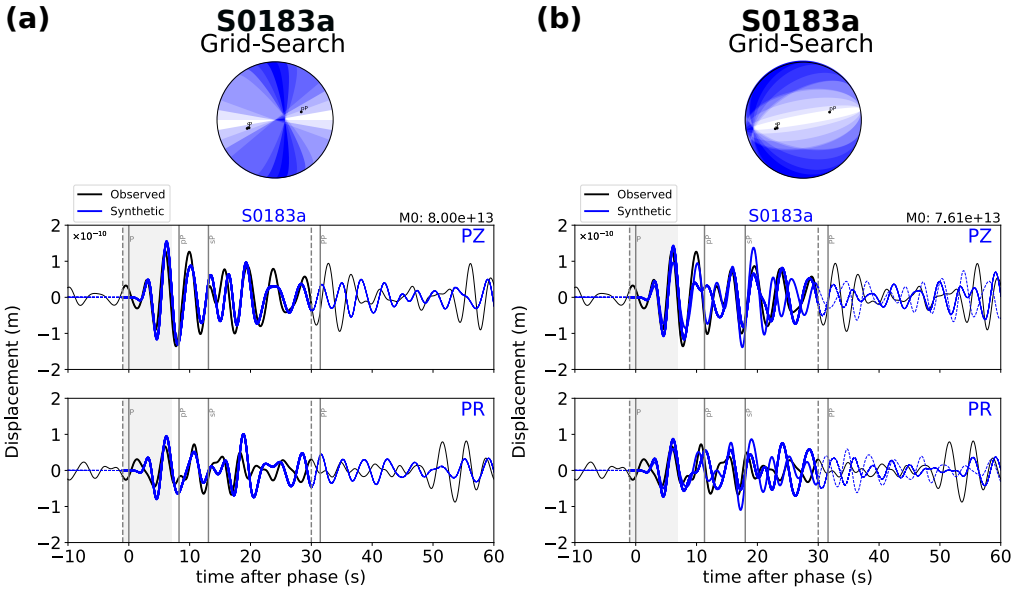

Figure C2. P wave inversion using a deep crustal model: Inversion results of the GS method using a 77 km crustal model. Figure **(a)** and **(b)** show results computed at a depth of 29 km and 41 km, respectively. The probabilistic beachball and the waveform Figures are structured the same as in Figure 3a and 3b. The solid gray vertical lines denote the first arriving P and S phase and later arriving phases pP, sP and PP calculated using ray-tracing.

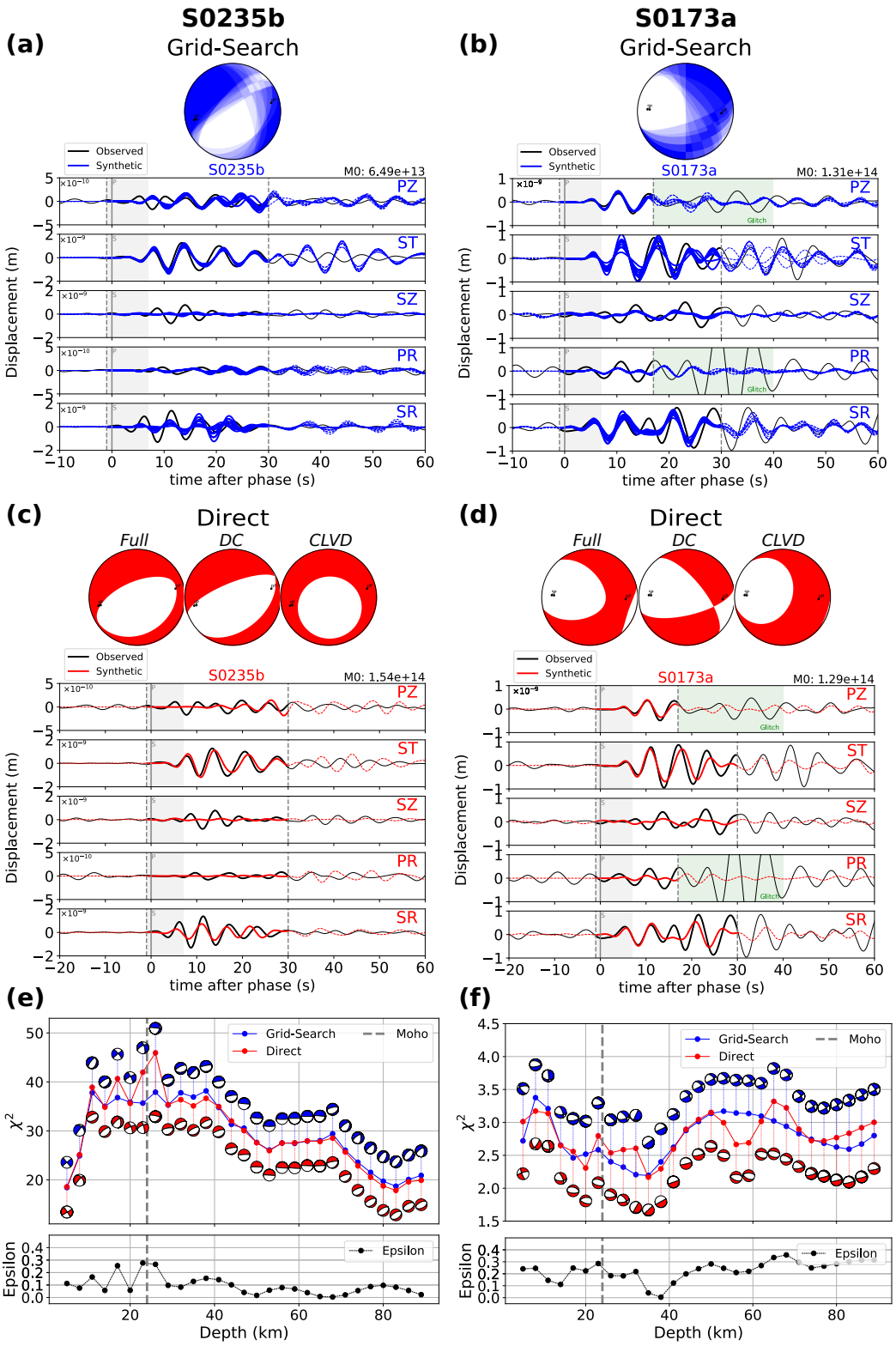

Figure C3. P and S wave inversion using a narrow band-pass: Inversion results of the direct inversion (red) and GS method (blue) using a 24 km crustal model. The corner frequencies of the band-pass are 0.125 Hz and 0.2 Hz. **(a,c)** and **(b,d)** show results computed at 47 km and 29 km depth, respectively. **a-f** contain the same plot structure as in Figure 3.

Acknowledgments

N.B was funded for this research by ETH grant 1-003285-000. We acknowledge NASA, CNES, their partner agencies and Institutions (UKSA, SSO, DLR, JPL, IPGP-CNRS, ETHZ, IC, MPS-MPG) and the flight operations team at JPL, SISMOC, MSDS, IRIS-DMC and PDS for providing SEED SEIS data. We further acknowledge the MQS front-line and review team. The French co-authors acknowledge CNES and ANR (ANR-19-CE31-0008-08). Numerical simulations were supported by a grant from the Swiss National Supercomputing Centre (CSCS) under project ID s922. InSight seismic data presented here (http://dx.doi.org/10.18715/SEIS.INSIGHT.XB 2016) is publicly available through the Planetary Data System (PDS) Geosciences node, the Incorporated Research Institutions for Seismology (IRIS) Data Management Center under network code XB and through the Data center of Institut de Physique du Globe, Paris (http://seis-insight.eu). We thank the developers of Instaseis for sharing the broadband waveform database, which was essential for this work. This is InSight Contribution Number 180.

References

Banerdt, W. B., Smrekar, S. E., Banfield, D., Giardini, D., Golombek, M., Johnson, C. L., ... others (2020). Initial results from the insight mission on mars. *Nature Geoscience*, 1–7.

Böse, M., Clinton, J., Ceylan, S., Euchner, F., van Driel, M., Khan, A., ... Banerdt, W. (2017). A probabilistic framework for single-station location of seismicity on earth and mars. *Physics of the Earth and Planetary Interiors*, *262*, 48–65.

Ceylan, S., van Driel, M., Euchner, F., Khan, A., Clinton, J., Krischer, L., ... Giardini, D. (2017). From initial models of seismicity, structure and noise to synthetic seismograms for mars. *Space Science Reviews*, *211*(1-4), 595–610.

Clinton, J., Giardini, D., Böse, M., Ceylan, S., Van Driel, M., Euchner, F., ... others (2018). The marsquake service: Securing daily analysis of seis data and building the martian seismicity catalogue for insight. *Space Science Reviews*, *214*(8), 133.

Clinton, J. F., Giardini, D., Lognonné, P., Banerdt, B., van Driel, M., Drilleau, M., ... others (2017). Preparing for insight: An invitation to participate in a blind test for martian seismicity. *Seismological Research Letters*, *88*(5), 1290–1302.

Garcia, R., Schardong, L., & Chevrot, S. (2013, feb). A Nonlinear Method to Estimate Source Parameters, Amplitude, and Travel Times of Teleseismic Body Waves. *Bull. Seismol. Soc. Am.*, *103*(1), 268–282. Retrieved from `http://www.bssaonline.org/cgi/doi/10.1785/0120120160` doi: 10.1785/0120120160

Giardini, D., Boschi, E., & Palombo, B. (1993). Moment tensor inversion from mednet data (2) regional earthquakes of the mediterranean. *Geophysical research letters*, *20*(4), 273–276.

Giardini, D., Lognonné, P., Banerdt, W. B., Pike, W. T., Christensen, U., Ceylan, S., ... others (2020). The seismicity of mars. *Nature Geoscience*, *13*(3), 205–212.

Giardini, D., Malagnini, L., Palombo, B., & Boschi, E. (1994). Broad-band moment tensor inversion from single station, regional surface waves for the 1990, nw-iran earthquake sequence. *Annals of Geophysics*, *37*(6).

InSight Mars SEIS Data Service. (2019). *Seis raw data, insight mission.* IPGP, JPL, CNES, ETHZ, ICL, MPS, ISAE-Supaero, LPG, MFSC. Retrieved from `http://datacenter.ipgp.fr/networks/detail/XB_2016` doi: 10.18715/SEIS.INSIGHT.XB_2016

InSight Marsquake Service. (2020). *Mars seismic catalogue, insight mission; v2 2020-04-01.* ETHZ, IPGP, JPL, ICL, ISAE-Supaero, MPS, Univ. Bristol. Retrieved from `http://www.insight.ethz.ch/seismicity/catalog/v2` doi: 10.12686/a7

Jost, M. u., & Herrmann, R. (1989). A student's guide to and review of moment tensors. *Seismological Research Letters*, *60*(2), 37–57.

Kennett, B. L., Marson-Pidgeon, K., & Sambridge, M. (2000, oct). Seismic Source characterization using a neighbourhood algorithm. *Geophys. Res. Lett.*, *27*(20), 3401–3404. Retrieved from `http://www.agu.org/pubs/crossref/2000/2000GL011559.shtmlhttp://doi.wiley.com/10.1029/2000GL011559` doi: 10.1029/2000GL011559

Khan, A., & Connolly, J. (2008). Constraining the composition and thermal state of mars from inversion of geophysical data. *Journal of Geophysical Research: Planets*, *113*(E7).

Khan, A., Liebske, C., Rozel, A., Rivoldini, A., Nimmo, F., Connolly, J., ... Giardini, D. (2018). A geophysical perspective on the bulk composition of mars. *Journal of Geophysical Research: Planets*, *123*(2), 575–611.

Khan, A., van Driel, M., Böse, M., Giardini, D., Ceylan, S., Yan, J., ... others (2016). Single-station and single-event marsquake location and inversion for

structure using synthetic martian waveforms. *Physics of the Earth and Planetary Interiors*, *258*, 28–42.

Knapmeyer, M., Oberst, J., Hauber, E., Wählisch, M., Deuchler, C., & Wagner, R. (2006). Working models for spatial distribution and level of mars' seismicity. *Journal of Geophysical Research: Planets*, *111*(E11).

Knapmeyer, M., & Weber, R. (2010). Steps towards the determination of deep moonquake source orientations. In *European planetary science congress (epsc) 2010.* Retrieved from https://elib.dlr.de/65452/

Lognonné, P., Banerdt, W. B., Giardini, D., Pike, W. T., Christensen, U., Laudet, P., ... Wookey, J. (2019, January). SEIS: Insight's seismic experiment for internal structure of mars. *Space Science Reviews*, *215*(1). Retrieved from https://doi.org/10.1007/s11214-018-0574-6 doi: 10.1007/s11214-018-0574-6

Lognonné, P., Banerdt, W. B., Pike, W. T., Giardini, D., Christensen, U., Garcia, R. F., ... Zweifel, P. (2020). Constraints on the shallow elastic and anelastic structure of mars from InSight seismic data. , *13*(3), 213–220. Retrieved 2020-04-12, from https://www.nature.com/articles/s41561-020-0536-y (Number: 3 Publisher: Nature Publishing Group) doi: 10.1038/s41561-020-0536-y

Minson, S. E., & Dreger, D. S. (2008). Stable inversions for complete moment tensors. *Geophysical Journal International*, *174*(2), 585–592.

Nissen-Meyer, T., van Driel, M., Stähler, S. C., Hosseini, K., Hempel, S., Auer, L., ... Fournier, A. (2014). Axisem: broadband 3-d seismic wavefields in axisymmetric media. *Solid Earth*, *5*(1), 425.

Rivoldini, A., Van Hoolst, T., Verhoeven, O., Mocquet, A., & Dehant, V. (2011). Geodesy constraints on the interior structure and composition of mars. *Icarus*, *213*(2), 451–472.

Roberts, G. P., Matthews, B., Bristow, C., Guerrieri, L., & Vetterlein, J. (2012, feb). Possible evidence of paleomarsquakes from fallen boulder populations, Cerberus Fossae, Mars. *J. Geophys. Res. Planets*, *117*(E2), n/a–n/a. Retrieved from http://doi.wiley.com/10.1029/2011JE003816 doi: 10.1029/2011JE003816

Scholz, J.-R., Widmer-Schnidrig, R., Davis, P., Lognonne, P., Pinot, B., Garcia, R. F., ... Banerdt, W. B. (2020). Detection, analysis and removal of glitches from InSight's seismic data from Mars. *Journal of Geophysical Research: Planets*, *submitted*.

Stähler, S., & Sigloch, K. (2014). Fully probabilistic seismic source inversion-part 1: Efficient parameterisation. *Solid Earth*(2), 1055–1069.

Stähler, S. C., & Sigloch, K. (2016). Fully probabilistic seismic source inversion–part 2: Modelling errors and station covariances.

Taylor, J., Teanby, N. A., & Wookey, J. (2013). Estimates of seismic activity in the cerberus fossae region of mars. , *118*(12), 2570–2581. Retrieved 2020-04-30, from https://agupubs.onlinelibrary.wiley.com/doi/abs/10.1002/2013JE004469 (_eprint: https://agupubs.onlinelibrary.wiley.com/doi/pdf/10.1002/2013JE004469) doi: 10.1002/2013JE004469

Vallée, M., Charléty, J., Ferreira, A. M. G., Delouis, B., & Vergoz, J. (2011, jan). SCARDEC: a new technique for the rapid determination of seismic moment magnitude, focal mechanism and source time functions for large earthquakes using body-wave deconvolution. *Geophys. J. Int.*, *184*(1), 338–358. Retrieved from http://doi.wiley.com/10.1111/j.1365-246X.2010.04836.x doi: 10.1111/j.1365-246X.2010.04836.x

Van Driel, M., Krischer, L., Stähler, S. C., Hosseini, K., & Nissen-Meyer, T. (2015). Instaseis: Instant global seismograms based on a broadband waveform database. *Solid Earth*, *6*(2), 701.